

Ultrasonic Holography Techniques for Localizing and Imaging Solid Objects

Alois C. Knoll, *Member, IEEE*

Abstract—Ultrasonic holographic imaging holds the potential for recognizing object contours in two-dimensional or three-dimensional space. The theory of both the monofrequency and multifrequency modes of the method, as suitable for the requirements of object recognition in robot assembly tasks, is described. The theory was implemented experimentally. Results obtained show that the monofrequency approach provides fairly good lateral but insufficient depth resolution. By contrast, with multifrequency holography, depth resolutions of better than 3 mm and lateral resolutions of about 10 mm are attainable. New ultrasonic transducers, combined with a special signal preprocessing procedure, are a prerequisite for resolutions of this order. Typical images as obtained from several test scenes are presented. Suitable applications and possible future research are briefly outlined.

I. INTRODUCTION

IN recent years, noncontact sensing based on ultrasonics has increasingly attracted attention in the robotics community. Ultrasonic sensors provide accurate distance measurement at low cost, are simple in construction, and are mechanically robust. Often they can be used in environments where other sensors tend to fail. Moreover, the basic arrangement is very simple: An ultrasonic transmitter generates a short sound impulse causing a longitudinal wave to propagate away from the sensor. This wave is reflected by solid objects and travels back to the sensor waiting for the return echo. Upon reception of the echo, the time of flight is determined. Multiplication of this time period by the sound velocity yields the distance between the sensor and the reflector.

In spite of this straightforward principle, and other advantages, the range of applications of these sensors has remained rather narrow [1], [2]. This may be due to several shortcomings partly inherent to the physics of ultrasound propagating in air but also to properties specific to commonly available sonar range meters: Sensors are easily misled by multiple reflections occurring even in moderately complex environments. For example, erroneous outputs are frequently observed in the presence of ambient noise, air currents, and thermal variations; objects exhibiting specular surfaces not orthogonal to sound propagation cannot be detected because such surfaces reflect the signal energy away from the point-like receiver. For robot assembly tasks, however, the most severe restriction is poor spatial resolution. Mostly for this reason, ultrasonic sensors have widely been regarded as unsuitable for object recognition requiring the separation of

different objects or of fine object details on the order of centimeters or below.

The vast majority of applications may be found in the realm of mobile robots [3]–[8]. For purposes of obstacle avoidance and guidance control, ultrasonic sensors circumventing many of the aforementioned disadvantages may be designed. Typical designs include horn-like rotating sensor devices or arrangements of several independent one-dimensional sonars. Other approaches use mechanical scanners or electronically deflected arrays of ultrasonic transducers transmitting into different directions and receiving echoes by a single wide-angle receiver. The data acquired may be used to generate a coarse image of the world surrounding the sensor.

These designs, along with a number of attempts to introduce other sensor concepts employing different principles [9]–[19], aim primarily at extending the spatial field of view of the sensor in the lateral direction, i.e., perpendicular to the direction of sound propagation. In the axial direction, however, sensors based on standard sonars [20] permit the detection of only the closest reflector with respect to the direction of sound propagation (axial or depth direction). Objects behind this first reflector will not be recognized because the timer of the sensor is stopped after the reception of the first partial echo exceeding a certain threshold. All echoes that are reflected by objects farther away and thus arrive later are discarded. Although easy to implement, this procedure provides only a fraction of the information about the environment contained in the entirety of all echoes. It is obviously desirable for a powerful sensor for object recognition to make available as much information about the object structure, including axial information, as is possible. The latter may be derived from the return signal if the echo sequence returning to the receiver is recorded over a certain period of time by means of a transient recorder [21], [22]. The complete signal may then be examined even for faint echoes.

Acoustical holography holds the potential for exploiting all information in both the axial and lateral directions, thereby making the generation of comparatively high-resolution images possible. This method has been used successfully in the area of nondestructive evaluation (NDE) as well as medical and underwater marine applications for detecting, localizing, and tracking objects [23]–[29]. By contrast, our work has focussed on adapting holography to the needs of robotics where the determination of the shape and structure of objects is of primary interest. Sensor and object geometry also differ significantly from NDE as do the requirements for speed, resolution, transducer properties, waveform of irradiating signals, and workspace dimensions.

Manuscript received October 12, 1989; revised December 17, 1990.

The author is with the Technische Universität Berlin, W-1000 Berlin, Germany.

IEEE Log Number 9144460.

1042-296X/91/0800-0449\$01.00 ©1991 IEEE

In this paper we briefly review the theory underlying the holographic approach for both monofrequency and multifrequency sound signals. Based on the resulting mathematical relations, possible implementations of the holographic method are discussed. A specially developed ultrasonic transducer and a signal preprocessing algorithm are presented. The experimental setup is described along with results achieved for some objects. We conclude with an assessment of the benefits of the method and an outline for possible future research.

II. METHOD

The purpose of holography, optical or acoustical, is the reconstruction of wavefronts based on the knowledge of their phase and amplitude distribution on a prescribed surface. It is a two-step process: recording and subsequent reconstruction. The stored representation of the phase and amplitude distribution is called a hologram. If the recording is done on a two-dimensional surface, reconstruction is possible for three-dimensional space. Likewise, if reconstruction is desired for a plane, recordings need only be taken along a line [24], [26], [31]. Object recognition follows the reconstruction step in the following way: At all points where a sound source or a reflector is located, the magnitude of the reconstructed wave field takes on high values; at other points, its magnitude is low. Suitable thresholding therefore isolates the contours of the objects inside the reconstruction region.

The process of wavefront reconstruction is easy to understand if one recalls the Huygens-Fresnel principle of wave propagation: Every point of a wavefront may be regarded as the center of a secondary elementary wavelet; the superposition of all of these wavelets constitutes the wavefront at any point in space. Ideally, upon completion of the recording step, the amplitude and phase of all elementary wavelets emanating from the recording surface are known. By means of transmitters generating elementary waves of exactly the phase and amplitude registered during recording, the original wavefront may be reproduced physically. In our context, rather than generating a replica of the wavefield, the knowledge of its magnitude distribution at the time of recording is of primary interest. Therefore, the reconstruction of the field is carried out numerically, yielding a set of values representing its magnitude.

For many applications in robotics, two-dimensional (axial and lateral) recognition of object structures will be adequate. Since it is obviously much easier to realize in practice than full three-dimensional recognition, we will restrict our attention to the two-dimensional planar case. Here, both the object and the field have no structure perpendicular to the (x, z) plane (see Fig. 1). Their long dimension extends infinitely both in the positive and negative y direction. Therefore, a single cross section at $y = 0$ defines the entire cylindrical object. The sound field is also independent of the y coordinate and it may be recorded completely along a line in the (x, z) plane.

This model is sufficient for objects that have little or no structure in the y direction or for focusing transducers whose radiation patterns are narrow in the y direction and thus

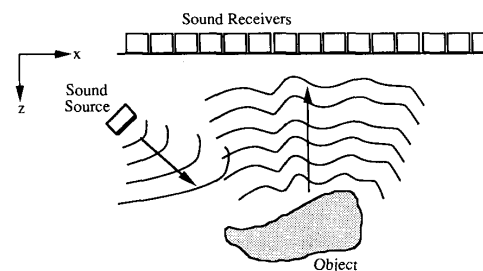


Fig. 1. Principle of holographic recording in reflection mode.

illuminate only a small stripe of the object. Mathematically, the extension to three dimensions is simple and requires only minor modifications, but for true three-dimensional imaging, the sound field varies in the y direction as well and must therefore be recorded on a surface, not just along a line. The differences between the two-dimensional and the general three-dimensional case will be mentioned as the theory is developed below.

A. Monofrequency Holography

In the case of monofrequency holography, stationary sound wavefields of a single frequency, which remains constant over time, are recorded and reconstructed. To generate an image of the object's shape, the sound field inside the object plane is computed based on the data recorded on the aperture. A plot of the sound field magnitude in the object plane then renders an image of the object contours.

With reflection-mode holography, an ultrasonic transducer emitting a sinusoidal wave irradiates the object to be analyzed (Fig. 1). Reflection at an object causes a certain fraction of the sound energy to be scattered back to the aperture where the recording takes place. All object points occur at a constant depth z_0 while the aperture of length D is assumed to be at $z = 0$ (Fig. 2). At any point, the sound wavefield of wavelength λ is completely defined by a complex-valued function $\Phi(x, z)$.

The phase and amplitude of $\Phi(x, z)$ are defined with respect to amplitude and phase of the transmitted signal acting as a constant reference. As mentioned above, the goal of numerical reconstruction is to compute the magnitude $|\Phi(x, z)|$ inside the (x, z) plane. It is clear that this can be done only for a finite set of points. If the sound field is to be recorded completely, it is necessary that the receiving device be able to measure both the phase and amplitude of Φ . They can be measured directly only if the relationship between the acoustical input and the electrical output of the receiving element is linear. This linearity requirement is met by acoustical transducers.

Unambiguous reconstruction is possible only for spatial regions that do not contain sound sources or inside which the exact location and strength of sound sources are known [30], [31]. In our context, the half-space $z \leq 0$ meets this requirement while the half-space $z > 0$, which contains the object, does not. It is obvious that the position and strength of the sound sources are difficult, if not impossible, to determine if only the field distribution on the aperture is known because

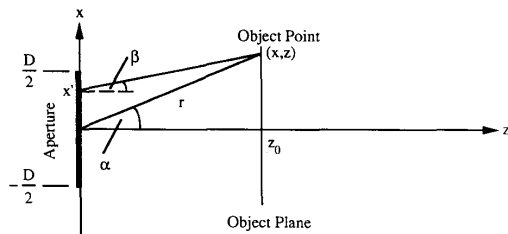


Fig. 2. Geometry for monofrequency holography.

different sources may generate identical field distributions. It can be shown, however, that even on half-space $z > 0$ an exact reconstruction is possible for all points within the region $0 \leq z < z_0$, where z_0 denotes the depth of the object point closest to the aperture (see [31, p. 37]). Consequently, monofrequency holography is appropriate only for the recognition of objects not extensively structured in the depth (axial) direction.

With these principal limitations in mind, we now derive the reconstruction formula and in the process establish the relevant mathematical nomenclature. Subsequently, we will show how it must be modified for implementation on a digital computer. The distribution of sound wavefields $\Phi(x, z)$ in air is governed by the fundamental scalar wave equation [32]. In the monochromatic (single frequency) case, the time dependency is assumed to be $e^{j\omega t}$ at any point in space; it will henceforth be dropped. It follows directly that in the source-free regions the sound field is given by

$$\Delta\Phi(x, z) + k^2\Phi(x, z) = 0 \quad (1)$$

where $k = 2\pi/\lambda = \omega/c$ is the wavenumber, and c the speed of propagation. Solving (1) for Φ compatible with boundary conditions imposed by the object yields the desired field distribution. In our context, however, the structure of the object is unknown, and only the sound field on the linear aperture is given. Thus, it is necessary to transform (1) using Green's theorem to obtain our basic reconstruction formula

$$\Phi(x, z) = \frac{k}{2} j \int_{-\infty}^{\infty} \Phi(x', 0) \frac{z}{\sqrt{(x-x')^2 + z^2}} \cdot H_1^{(1)}\left(k\sqrt{(x-x')^2 + z^2}\right) dx' \quad (2)$$

where $\Phi(x', 0)$ denotes the strength of the complex sound field measured on the aperture. $H_1^{(1)}$ is Hankel's function of the first kind and the first order, describing the phase and amplitude dependence of converging waves propagating from the object to the aperture. In principle, these waves are weighted by the strength $\Phi(x', 0)$ on the aperture and superposed by taking the integral over the aperture to form the resulting wave field. Their amplitude is reduced by an obliquity factor that is the cosine of angle β that the incident wave makes with the normal of the aperture (see Fig. 2). In the above equation this cosine is represented by the quotient $z/\sqrt{(x-x')^2 + z^2}$.

In the case of three-dimensional reconstruction, the sound

field $\Phi(x', y', 0)$ must be recorded on an aperture surface. Then, $\Phi(x, y, z)$ is computed by taking the double integral over x' and y' . The integrand consists of $\Phi(x', y', 0)$, as before multiplied by $\cos \beta$, and a function $e^{jk r_1}/r_1$ replacing the Hankel function and describing the propagation of spherical waves converging toward the aperture. The distance term $r_1 = \sqrt{(x-x')^2 + (y-y')^2 + z^2}$ now also depends on the y coordinate (see [33, p. 40] for a full derivation).

Since the evaluation of (2) for the entire region $0 \leq z < z_0$ is cumbersome and in most cases unnecessary, we will restrict ourselves to an approximate solution in the paraxial area where $x \ll z$ and hence $r = \sqrt{x^2 + z^2} \approx z$. Then, $H_1^{(1)}$ can be replaced by its asymptotic approximation

$$H_1^{(1)}(x) \approx \sqrt{\frac{1}{\pi x}} e^{j(x-(3/4)\pi)} \quad (3)$$

and, using $r^2 = x^2 + z^2$, the distance term becomes

$$\begin{aligned} \sqrt{(x-x')^2 + z^2} &= r \sqrt{1 - \frac{2xx'}{r^2} + \left(\frac{x'}{r}\right)^2} \\ &\approx r \left[1 - \frac{xx'}{r^2} + \frac{1}{2} \left(\frac{x'}{r}\right)^2 \left(1 - \frac{x^2}{r^2}\right) \right]. \end{aligned} \quad (4)$$

Substituting (3) and (4) into (2) we obtain

$$\Phi(x, z) = j \frac{z}{\sqrt{\lambda r^3}} e^{j(kr-(3/4)\pi)} \int_{-\infty}^{\infty} \Phi(x', 0) \cdot e^{-jk(xx'/r - x'^2/(2r)(1-x^2/r^2))} dx'. \quad (5)$$

For notational convenience, we substitute $\sin \alpha = x/r$ and $\cos \alpha = z/r$ into (5) and get

$$\Phi(x, z) = \frac{\cos \alpha}{\sqrt{\lambda r}} e^{j(kr-(1/4)\pi)} \int_{-\infty}^{\infty} \Phi(x', 0) \cdot e^{-jk(x' \sin \alpha - x'^2/(2r) \cos^2 \alpha)} dx' \quad (6)$$

with the angle α shown in Fig. 2. Assuming that α in the exponent of (6) varies only slightly, $\cos \alpha$ can be replaced by a constant C_0 . Apart from the remaining quadratic phase factor, the field distribution at z_0 may now be considered a Fourier transform of the field distribution measured on the aperture. Recalling our supposition $x \ll z$, we can let C_0 equal unity. Note that these approximations apply to the three-dimensional case as well. To obtain the three-dimensional version of (6), it is necessary to add the y coordinate to the integrand and take the double integral. The only important difference is the dependence on distance: The $1/\sqrt{\lambda r}$ dependence in the two-dimensional case becomes a $1/\lambda r$ dependence in the three dimensional case.

Defining a spatial frequency

$$f_x = \frac{1}{\lambda} \sin \alpha = \frac{1}{\lambda} \frac{x}{r} \quad (7)$$

leads to our final result

$$|\Phi(f_x, z)| = C_1(f_x, z) \left| \int_{-\infty}^{\infty} (\Phi(x', 0) e^{jkx'^2/(2z)}) \cdot e^{-j2\pi f_x x'} dx' \right| \quad (8)$$

where

$$C_1(f_x, z) = \frac{\sqrt{1 - \lambda^2 f_x^2}}{\sqrt{\lambda z}}$$

Equation (8) makes it possible to calculate the magnitude of the sound field in the region $0 \leq z < z_0$ based solely on measurements of the field $\Phi(x', 0)$ along the linear aperture.

In the remainder of this section we transform (8) into a discretized form suitable for a practical imaging system where the recording aperture is limited to a finite length D (see Fig. 2). Not only are apertures of infinite length impossible in reality, but the attenuation of sound in air also makes the reception of any measurable return echo on aperture points beyond a certain distance impossible. By limiting the recording to $\pm D/2$, wave components arriving at aperture points beyond this limit are ignored. They would otherwise contribute to the resulting field. It is obvious that this loss of information alters the reconstruction behavior of the system; for an analysis of the resulting effects, see [34]. Furthermore, it is impossible to record the sound field at every single point of the interval $[-D/2, +D/2]$. Instead, a finite number of samples must be taken by a finite number of fixed transducers (or one movable transducer) along the aperture. For this reason the aperture is divided into a number of intervals each contributing one element to the finite set of samples. Because of the interval $[-D/2, +D/2]$. Instead, a finite number of samples must be taken by a finite number of fixed transducers

$$F_m = \frac{1}{N} \sum_{n=0}^{N-1} f_n e^{-j2\pi(nm/N)} \quad (9)$$

where $m = 0 \cdots N - 1$.

To adapt (8) to these constraints, the limits of integration of the integral in (8) are changed from $x' = -\infty \cdots +\infty$ to $x' = -D/2 \cdots D/2$ (Fig 2). In a second step, by a change of variables, the range of integration is mapped to $x = 0 \cdots D$:

$$|\Phi(f_x, z)| = C_1(f_x, z) \left| \int_0^D \Phi\left(x - \frac{D}{2}, 0\right) \cdot e^{jk(x-D/2)^2/(2z)} e^{-j2\pi f_x(x-D/2)} dx \right| \quad (10)$$

Dividing the integral over $[0, D]$ into N subintegrals each covering a subinterval length $h = D/N$ greater than or equal to the spatial extent of the transducer's active area yields:

$$|\Phi(f_x, z)| = C_1(f_x, z) \left| \sum_{n=0}^{N-1} \int_{x=nh}^{(n+1)h} w(x) \Phi\left(x - \frac{D}{2}, 0\right) \cdot e^{jk(x-D/2)^2/(2z)} e^{-j2\pi f_x(x-D/2)} dx \right| \quad (11)$$

where a windowing function $w(x)$ has been introduced to accommodate situations where the recording area inside a subinterval is smaller than h . If this is so, $w(x)$ is equal to unity where the recording takes place and zero otherwise. In practice, the correct evaluation of the subintegral in (11) is not possible because the sound field distribution cannot be mapped to a spatially continuous electrical signal. The ultrasonic transducer must have some spatial extent to pick up enough sound energy, but it outputs only a single time-varying electrical signal representing the result of some kind of unavoidable averaging over the active area. To minimize the discrepancy between the true field and the output of the transducer, h must be small. Assuming that there is no gap between the transducers (which means that $w(x)$ equals unity and can be dropped) or, if there is a gap, that h is still small enough, we may take the one value the transducer outputs as valid for the entire subinterval. Then, the integrand in (11) may be considered constant over the integration interval, and we find that

$$|\Phi(f_x, z)| = C_1(f_x, z) \frac{D}{N} \left| \sum_{n=0}^{N-1} \Phi\left(\frac{nD}{N} - \frac{D}{2}, 0\right) \cdot e^{jk/(2z)(nD/N - D/2)^2} e^{-j2\pi f_x n(D/N)} \right| \quad (12)$$

Several comments about the size of h are in order at this point. Given our geometry where $x \ll z$ and given the amplitude dependence of $1/\sqrt{z}$, it is clear that phase changes are the crucial part in our approximation. It must be ensured that these changes are small inside the subintervals. If we consider the terms containing $f_x x$ in the exponential functions in (11), this requires that $f_x h \ll 1$. From our supposition $x \ll z$ it follows that $f_x \lambda \ll 1$. Hence, a reasonable requirement for h is that it not be greater than λ . Then, the electrical signal of the transducer may be seen as an approximate mapping of the real value of the sound field. For an analysis of geometries with transducers spaced farther apart, where only sparse data can be collected, see [34] and [35]; a detailed treatment of related problems can be found in [36].

Finally, we let $m = f_x/D$. This allows reconstruction to be performed only for discrete frequencies $f_x = m/D$. The index m must be constrained to values giving a positive radicand in the numerator of (12). Now, (12) can be rewritten to yield our final discretized result for the monofrequency case:

$$\left| \Phi\left(f_x = \frac{m}{D}, z\right) \right| = \frac{\sqrt{1 - \lambda^2 m^2}}{\sqrt{\lambda z}} \frac{D}{N} \left| \sum_{n=0}^{N-1} \Phi\left(\frac{nD}{N} - \frac{D}{2}, 0\right) \cdot e^{jk/(2z)(nD/N - D/2)^2} e^{-j2\pi(nm/N)} \right| \quad (13)$$

Absolute values of m greater than D/λ have no physical significance. For negative spatial frequencies $|\Phi(f_x =$

$m/D, z)$ can be computed using $F_{-m} = F_{N-m}$. As desired, the structure of (11) exactly matches that of (8) where coefficients f_n are found by inspection

$$f_n = \Phi \left(\frac{nD}{N} - \frac{D}{2}, 0 \right) e^{jk/(2z)(nD/N - D/2)^2}. \quad (14)$$

To summarize, monofrequency holography, as described above, proceeds as follows:

- Step 1:** Record the sound wavefield $\Phi(x, 0)$ on discrete points along the aperture.
Step 2: Multiply all of the recorded values by a quadratic phase factor according to (14).
Step 3: Fourier transform.
Step 4: Take absolute values of the Fourier transform and multiply by the factor in (13) to yield the sound field magnitude depending on spatial frequency and depth. Using (7), spatial frequencies can be related to absolute coordinate space.

Note that the data volume obtained from the first step is comparatively small: One complex number on each of, say, 512 aperture points results in a data volume of only 4 kbyte.

The above algorithm was evaluated experimentally; some of the results achieved will be presented in Section IV. It became clear from the experiments that lateral resolution is fairly good, but axial resolution is poor. The reason for this is easy to see: Spatial attenuation of the field of a sound source is $1/\sqrt{r}$ in the two-dimensional case and $1/r$ in the three-dimensional case where r is the distance between the observation point and the source (see (6)). However, to obtain depth information, it is desirable that the field magnitude be different from zero only at the point of the source. To provide such a sharp transition, it is necessary to use time-dependent impulses with short rise and fall times. We extend the results of monofrequency illumination to pulsed illumination after a brief discussion of the influence of object texture on the reflected field.

B. The Influence of Object Surface Texture

Up to this point our discussion has been confined to the sound field received at the aperture; thus it has not been necessary to make any assumptions about the object surface texture and its reflection properties. However, it is obvious that the structure of the object surface affects the way an incident sound wave is scattered back from the object and seen at the receivers of the imaging system: Unlike an unstructured object surface, a "rough" surface tends to scatter the wave thereby reducing the strength of the field picked up at the receiver. There is no difficulty when surface variations are small compared with the wavelength λ of the incident wave, i.e., when the surface is smooth. In this case the solid object acts like an optical mirror, which reflects most of the energy in one distinct direction, thus producing a high field strength for the reflected wave arriving at the aperture. Provided insonification is strong enough, this permits an easy application of (13) for further processing. At the other extreme, there is also no difficulty when surface changes

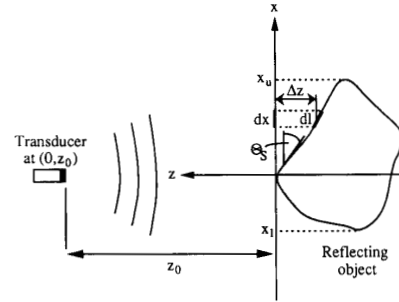


Fig. 3. Basic geometry and nomenclature for determining the reflection of sound waves by solids of arbitrary shape.

are larger than the resolution limit of the imaging system; in this case the structure of the object is also correctly resolved.

We now briefly explore how the strength of the echo is affected when surface variations lie somewhere between these two bounds: The object surface varies regularly or irregularly with an amplitude smaller than the resolution limit of the imaging system; the surface, however, is not smooth enough to be considered a mirror. Assuming again that the object has no structure in the y direction, we adopt the model developed in [37], [38] for the monofrequent reflection from irregular bodies. This model permits the computation of the ultrasonic echo from the body in terms of a calibration echo Φ_{cal} arriving at the receiver when a small plane calibration reflector arranged normal to the direction of sound propagation is used. We restrict ourselves to the geometry shown in Fig. 3 where both the transmitter and the receiver are located at $(0, z_0)$ with the origin of the coordinate system being one of the object surface points. If the transducers are sufficiently far from the projection of the surface onto the x axis, i.e., $(x_u - x_l) \gg z_0$, the incident wave can be considered to be plane and it can be shown [38], [39] that the sound field received at $(0, z_0)$

$$\Phi_r(f) = \frac{\Phi_{\text{cal}}(f)}{R_0 L_{\text{cal}}} \int_{x=x_l}^{x_u} R(\Theta_s) e^{-jk2\Delta z} dx \quad (15)$$

where $\Phi_r(f)$ denotes the reflected wave field seen at the receiver as a function of frequency f or wave number $k = 2\pi f/c$, respectively. Φ_{cal} is the sound field received when a small plane reflector with a smooth surface and length $L_{\text{cal}} = x_u - x_l$ is used where $x_l = -x_u$. Δz represents the distance between the surface contour elements dl and the wave plane at $z = 0$ (the maximum of Δz must be much smaller than z_0). $R(\Theta_s)$ is an angle-dependent reflection coefficient of the surface that remains inside the integrand because it varies along the contour as every contour element makes its own particular angle Θ_s with the waveplane. R_0 is the uniform reflection coefficient of the calibration reflector whose $\Theta_s = 0$.

As can be seen from (15), the field reflected by the object surface is composed of elemental contributions from projections dx of the surface contour elements dl onto the wave plane at $z = 0$. The round-trip distance $2\Delta z$ between dx and dl simply changes the phase angle of the elemental

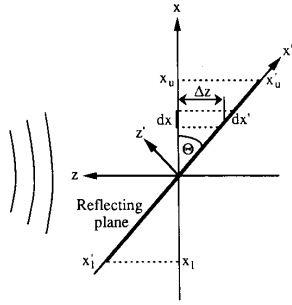
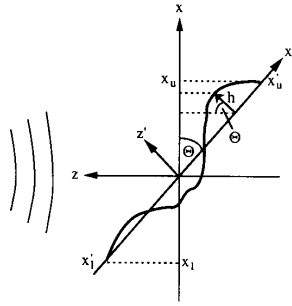


Fig. 4. Reflection from a smooth plane.

Fig. 5. A rough surface may be characterized by an elevation height h above a mean plane inclined at a fixed angle Θ .

wavelets traveling between $z = 0$ and the object surface and, hence, the phase angle of the complex quantity Φ_{cal} . Since $\max(\Delta z) \ll z_0$ the attenuation caused by propagation along $2\Delta z$ is neglected. We illustrate the use of (15) by analyzing the wave field reflected from a smooth plane reflector inclined at a fixed angle Θ (see Fig. 4) with the reflector being part of the x' axis of a rotated coordinate system (x', z') . Assuming a constant reflection coefficient $R(\Theta)$, (15) becomes

$$\Phi_{r_{\text{plane}}}(f) = \frac{\Phi_{\text{cal}}(f)R(\Theta)}{R_0 L_{\text{cal}}} \int_{x_l}^{x_u} e^{-jk2\Delta z} dx. \quad (16)$$

After a substitution $x = x' \cos \Theta$ and $\Delta z = x' \sin \Theta$, we have

$$\Phi_{r_{\text{plane}}}(f) = \frac{\Phi_{\text{cal}}(f)R(\Theta) \cos \Theta}{R_0 L_{\text{cal}}} \int_{x'_l}^{x'_u} e^{-jk2x' \sin \Theta} dx'. \quad (17)$$

Next, we shall explore a rough surface in general (see Fig. 5). Its roughness is characterized by a surface height coordinate h , relative to a mean plane $z' = 0$, and the angle-dependent reflection coefficient $R(\Theta_S)$, which varies along the x' axis [39]. The mean plane, as above, is inclined at an angle Θ . From elementary geometry it follows that $\Delta z = x' \sin \Theta - h \cos \Theta$ and that $x = x' \cos \Theta + h \sin \Theta$. Substituting for x and Δz in (15) yields

$$\Phi_{r_{\text{rough}}}(f) = \frac{\Phi_{\text{cal}}(f)}{R_0 L_{\text{cal}}} \int_{x'_l}^{x'_u} R(\Theta_S) \left(\cos \Theta + \frac{dh(x')}{dx'} \sin \Theta \right) \cdot (e^{-jk2x' \sin \Theta} e^{-jk2h(x') \cos \Theta}) dx'. \quad (18)$$

This is as far as we can go without knowing anything about the shape of h and the reflection coefficient. In the important case of h being randomly distributed, however, further steps can be taken, and the mean value $E\{\Phi_{r_{\text{rough}}}(f)\}$ can be calculated. Assuming a normal distribution of h with variance σ^2 and zero mean, the probability density function of h is

$$p(h) = \frac{1}{\sigma\sqrt{2\pi}} e^{-h^2/(2\sigma^2)}. \quad (19)$$

If covariance contributions are assumed to be negligible, the mean value for $\Phi_{r_{\text{rough}}}(f)$ may be computed by using (18) by taking expectations of the factors of the integrand:

$$E\{\Phi_{r_{\text{rough}}}(f)\} = \frac{\Phi_{\text{cal}}(f)}{R_0 L_{\text{cal}}} \int_{x'_l}^{x'_u} E\{R(\Theta_S)\} \cdot E\left\{\left(\cos \Theta + \frac{dh(x')}{dx'} \sin \Theta\right)\right\} \cdot e^{-jk2x' \sin \Theta} E\{e^{-jk2h(x') \cos \Theta}\} dx'. \quad (20)$$

From the probability density function $p(h)$ it follows that $E\{dh/dx'\} = 0$. Since both positive and negative angles are equally probable, a reasonable estimator for $E\{R(\Theta_S)\}$ is $R(\Theta)$, the reflection coefficient of the mean plane. The expectation of the last factor in the integrand is (see [40, p.185])

$$E\{e^{-jk2h(x') \cos \Theta}\} = \int_{-\infty}^{+\infty} p(h) e^{-jk2h \cos \Theta} dh = e^{-(1/2)\sigma^2(2k \cos \Theta)^2}. \quad (21)$$

Substituting these results for the expectations in (20) yields our final result:

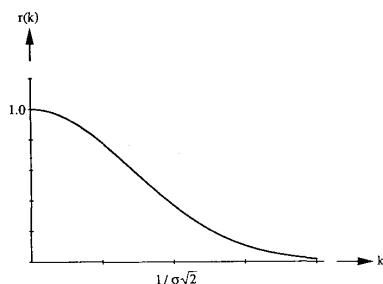
$$E\{\Phi_{r_{\text{rough}}}(f)\} = \frac{\Phi_{\text{cal}}(f)R(\Theta) \cos \Theta}{R_0 L_{\text{cal}}} \cdot e^{-(1/2)\sigma^2(2k \cos \Theta)^2} \int_{x'_l}^{x'_u} e^{-jk2x' \sin \Theta} dx'. \quad (22)$$

Hence, the expectation of the wave field returning from a randomly rough reflector is the same as the field reflected from the equivalent smooth reflector (see (17)) with $\sigma = 0$, multiplied by an exponential attenuation factor. If the surface in question is normal to sound propagation ($\Theta = 0$), then (22) can be simplified further giving

$$E\{\Phi_{r_{\text{rough}}}(f)\} = \frac{\Phi_{\text{cal}}(f)}{L_{\text{cal}}} (x'_u - x'_l) e^{-2\sigma^2 k^2}. \quad (23)$$

The form of the "roughness factor" $r(f) = e^{-2\sigma^2 k^2}$ is shown in Fig. 6.

This comparatively simple model is limited to the determination of the field at a single receiver; it does not permit the computation of the field distribution on a long aperture (for a detailed analysis of that problem, the reader is referred to [41]). The model is, however, useful for understanding how surface texture and inclination affect the reflected field. The effect on the imaging system is obvious: As surface rough-

Fig. 6. Shape of the roughness factor $r(k)$ in (23).

ness increases, the strength of the scattered field at a receiver decreases until it falls below the thresholding level of the imaging system, rendering the surface invisible. If the field strength generated by a smooth body is known, the model may at least give an estimate of how rough the surface may get before becoming invisible and from what angle the object should be illuminated. With multifrequency holography (see the section below), the frequency value to be used in (15) is the center frequency of the transducers. If the bandwidth is so large that this is insufficient, a time-domain analysis may be carried out, essentially consisting of Fourier transforming (15) into the time domain. For experimental results illustrating the reflection from solid bodies and the influence of texture, see [37]–[39].

C. Multifrequency Holography

As opposed to monofrequency holography, multifrequency holography is based on signals that have a broad spectrum in the frequency domain, ideally unit impulses. The principle of illumination, however, is the same in both cases: A sound signal is emitted by an ultrasonic transducer, and the echo received from the reflective object is recorded along the aperture. Since the echo is now a function of time not known *a priori*, it is not sufficient to record the amplitude and phase of the returning signal at an arbitrary time. Instead, the return signal arriving at each aperture point must be recorded during the time interval between the emission of the pulse and the arrival of the echo from the object point farthest away from the point of recording.

Since the recording system is linear, superposition applies, and pulsed holography may be viewed as the superposition of monofrequency reconstructions. Thus, the illumination pulse is seen as a weighted linear combination of elementary sinusoids of different temporal frequency denoted by $\Phi(x, z; \omega)$. After reintroduction of the time dependency $e^{j\omega t}$, the Fourier integral establishes the relation between the sound field in the frequency domain and the time domain:

$$\Phi(x, z; t) = \frac{1}{2\pi} \int_{-\infty}^{\infty} \Phi(x, z; \omega) e^{j\omega t} d\omega. \quad (24)$$

For the reconstruction of each of the frequency components, the general reconstruction formula (2) will be used. $H_1^{(1)}$ is again approximated using (3) but the distance term $\rho = \sqrt{(x - x')^2 + z^2}$ (Fig. 7) is not changed. We obtain

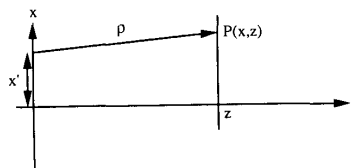


Fig. 7. Geometry for multifrequency holography.

from (2):

$$\Phi(x, z; \omega) = \frac{1}{\sqrt{j\lambda}} \int_{-\infty}^{\infty} \Phi(x', 0; \omega) \frac{e^{jk\rho}}{\sqrt{\rho}} \frac{z}{\rho} dx' \quad (25)$$

where the relation between k , ω , and λ is given by $\omega = kc = 2\pi c/\lambda$. Substituting (25) into (24) and rearranging gives

$$\Phi(x, z; t) = \frac{1}{2\pi} \int_{-\infty}^{\infty} \frac{z}{\rho\sqrt{\rho}} \left[\int_{-\infty}^{\infty} \frac{1}{\sqrt{j\lambda}} \Phi(x', 0; \omega) e^{j\omega(t+\rho/c)} d\omega \right] dx'. \quad (26)$$

The impulse is distorted by the multiplication of spectral components by a frequency-dependent factor. This is of minor interest, as is the distortion caused by dispersion in air; these two effects have only a minor influence on the impulse shape when compared to that of the ultrasonic transducers. The distorted impulse $\Phi'(x, z; t)$ can be computed for the time domain using (24):

$$\Phi'(x, z; t) = \frac{1}{2\pi} \int_{-\infty}^{\infty} \frac{1}{\sqrt{j\lambda}} \Phi(x, z; \omega) e^{j\omega t} d\omega. \quad (27)$$

Substituting (27) into (26), the result can be written as follows:

$$\Phi(x, z; t) = \int_{-\infty}^{\infty} \frac{z}{\rho\sqrt{\rho}} \Phi'(x', 0; t + \frac{\rho}{c}) dx'. \quad (28)$$

So the sound field can be calculated as a function of time on half-space $z \geq 0$ by a superposition of return signals on aperture points shifted by a propagation delay ρ/c .

The principle of the pulsed method is illustrated in Fig. 8: Suppose a reflector at point $P1$ was illuminated by the ultrasonic transmitter, and the reflection at $P1$ takes place at time $t = 0$. Then a pattern of impulse arrivals results on the aperture that uniquely identifies the echo as having come from point $P1$. To determine the spatial origin of the impulse as being $P1$, all recorded signals are shifted by a delay proportional to the distance between $P1$ and the points of the aperture. Then, they are summed up for the time $t = 0$. A resulting high amplitude indicates that there had been a reflection at $P1$. If, on the other hand, the impulse came from a different point $P2$, the shifts made for $P1$ will not match the actual delays, and the sum will be low.

In practice, the time that elapses between the emission of the impulse and its arrival at the point for which the sound field is computed must also be taken into account (see Section III). It is obvious that an evaluation of (28) cannot be made for all points in space; reconstruction must instead be limited to points within a suitably discretized grid. The granularity of this grid depends on the processing power available and on

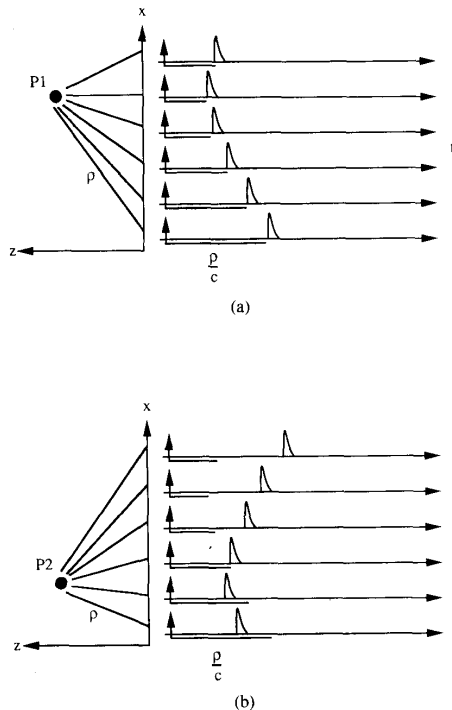


Fig. 8. Principle of multifrequency reconstruction. (a) Measured delay (as denoted by impulses on t axes) and delay calculated for point $P1$ (denoted by bar below the t axes) match. If impulses are shifted back by a time proportional to the length of the underbar and are summed up, a high value will result. (b) Summation based on delays for $P1$ will yield low sum if impulse emanated from $P2$.

the ability of transducers to discriminate between pulses arriving within short time intervals, i.e., the bandwidth of the transducers. It is important to note that the evaluation of the sound field amplitude may be carried out for all points (or, at least, clusters of points) in parallel, a necessary precondition for very fast recognition. Given an adequate parallel processor, recognition time will only depend on the propagation delay of sound in air. The algorithm for pulsed holography can now be formulated:

- Step 1: Emit a short sound impulse by a single transducer. Record transients $\Phi(x, 0; t)$ at different points x on the aperture.
- Step 2: Calculate the propagation delays (round trip time) for the spatial point where the sound field is to be computed.
- Step 3: Shift transients by a propagation delay proportional to distances. Subsequent addition yields the sound field strength for one spatial point.
- Step 4: Repeat steps 2 and 3 for all points (within the reconstruction grid).

Unlike monofrequency holography, this procedure will provide not only lateral but also axial information about the structure of the object. The penalty to pay is a much greater data volume (see Section III).

As mentioned before, the spatial resolution of the system

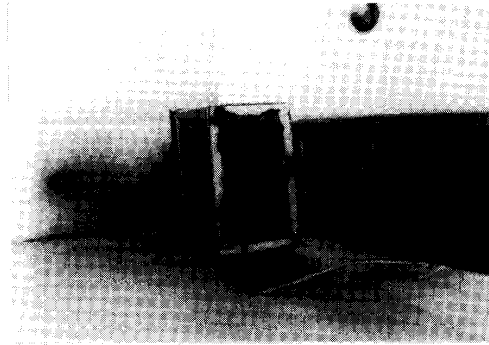


Fig. 9. L^2QZ transducer. Width is 2.8 cm and height is 4.2 cm.

in both the axial and the lateral direction directly depends on its ability to transmit short pulses and hence the bandwidth of the transfer channel (transmitter-air-receiver). As the bandwidth of standard ultrasonic transducers for air is by far too narrow to be used in pulsed holography, large-bandwidth ultrasonic transducers have been developed and realized as laboratory samples [42] (Fig. 9). Before proceeding to implementation issues of pulsed holography we briefly introduce these transducers and a specially developed signal preprocessing procedure.

III. IMPLEMENTATION

A. Broadband Transducers for Multifrequency Holography

Apart from a wide-band transfer function, development goals for these transducers included providing a field of view that is sufficiently large to be used for the illumination of medium-sized objects (extending up to several centimeters in the lateral direction), and making them rugged. The transducers realized (named L^2QZ for "low Q low Z ", low Q factor and low impedance) are composed of several alternating layers of electrically active piezoceramic material (thin foils of lead-zirconate-titanate, PZT) and plastics (Fig. 10). The former provides good electromechanical properties while the latter lowers the acoustic impedance of the entire element. The parameters of the plastics were chosen so as to come close to the acoustic impedance of air, resulting in a high coupling factor. The optimum thickness ratio of the layers was found to be $l_c/l_p = 0.01$ where the thickness of the entire element is $l = 5$ mm. The active element is surrounded by damping material that, in combination with the plastic foils, lowers the Q factor of the oscillating system and extends its bandwidth by flattening the transfer function. The low Q factor reduces efficiency, but the good coupling between the oscillator and air due to the low acoustic impedance partly compensates for this reduction.

The nominal operating frequency of the transducers is $f_0 = 200$ kHz. The bandwidth obtained is as large as 200 kHz with 6-dB limits being at 100 and 300 kHz. This must be compared to standard transducers for air, consisting of a monolithic block of piezoceramics, whose bandwidth is well below 10 kHz. An operating frequency of 200 kHz was selected as a compromise between attenuation in air and the minimum size of detectable objects. The frequency can be

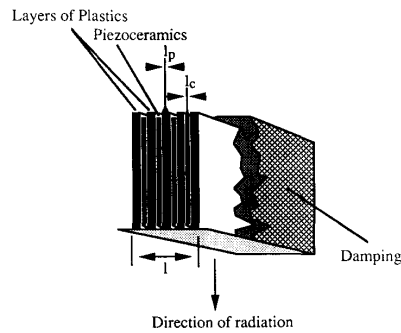


Fig. 10. Schematic representation and dimensions of L^2QZ transducer. l_c is thickness of piezoceramic layer, l_p thickness of plastics layer. Element width l is 5 mm.

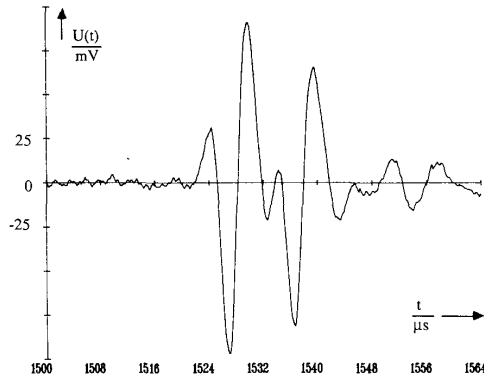


Fig. 11. Typical output signal of L^2QZ transducer. Signal returned from two reflectors 2 mm apart in depth direction (see Fig. 12).

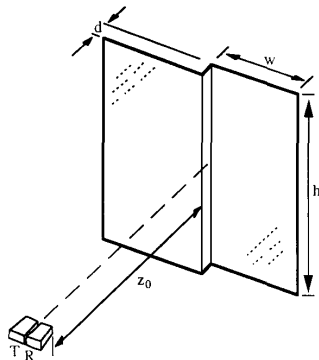


Fig. 12. Setup for obtaining the echo of Fig. 11. Step size $d = 2$ mm, height $h = 400$ mm, width $w = 150$ mm, and distance $z_0 = 250$ mm.

increased if the mechanical dimensions of the active element are reduced accordingly. The beam width of the main lobe is 15° and 5° in two orthogonal planes. The maximum distance between a medium-sized object and the transducer pair is approximately 0.5 m. Fig. 11 shows a real output signal of the receiving transducer. Two reflectors spaced 2 mm apart in the axial direction served as the object, which reflected a sound impulse emitted by an L^2QZ transmitter (see Fig. 12). The impulse applied to the transmitter was of nearly rectangular shape; its amplitude was 200 V, and its duration was 10 μs .

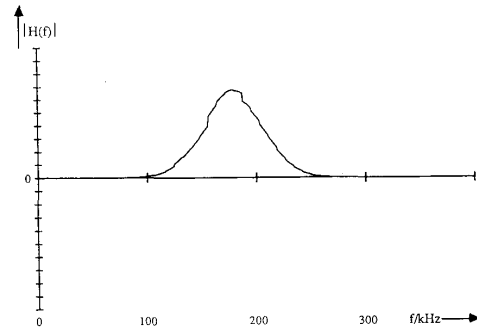


Fig. 13. Transfer function of L^2QZ transducers after windowing.

Before introducing the signal preprocessing procedure we take a brief look at the transmission channel. The channel may be thought of as consisting of three main components affecting the shape of the signal on its way from the pulse generator to the output of the receiving transducer. These components are the ultrasonic transducers, the propagation medium air, and the reflector, all of which are assumed to be linear.

The effects of pulse distortion caused by propagation and by dispersion in air will not be considered. They are clearly negligible when compared to the influence of the transducers on the shape of the signal. Consequently, the transfer function of the medium is simply a constant attenuation combined with a constant propagation delay (for a fixed distance between transducers and object). The reflecting areas of the object, likewise, are modeled as generating time-delayed and attenuated replicas of the impulse arriving at the surface of the object. The transducers act as bandpasses with a center frequency equal to the resonance frequency of the mechanical oscillator (for a theoretical treatment of their properties see [43, p. 353]; for transfer functions of common piezoelectric transducers, see [44]).

To suppress undesirable contributions to the signal from frequency ranges far off the center frequency (L^2QZ transducers are also sensitive to very low frequencies), the received signal is windowed. In our case, a Gaussian window was chosen. The modulus of the transfer function of the L^2QZ transducer after multiplication by such a window is shown in Fig. 13. This type of window was selected first of all because its shape is similar to the theoretical shape of the transfer function of the transducers; secondly, it does not introduce overshoots into the signal; and, finally, its mathematical treatment is easy. The combination of the L^2QZ transducer and the Gaussian window will henceforth be modeled as a Gaussian bandpass with center frequency f_0 and a constant group delay t_0 . The deviations from the ideal Gaussian shape are neglected. Since the whole system is linear and superposition applies, both transducers (L^2QZ transmitter and receiver) are combined to form a single bandpass.

We shall now introduce the signal preprocessing procedure we utilized. It is easy to show that the response of the Gaussian bandpass with center frequency f_0 , when excited

by a unit impulse $\delta(t)$ is

$$g(t) = a \cos(2\pi f_0[t - t_0])e^{-(t-t_0)^2/\tau_0^2} \quad (29)$$

where a is an arbitrary gain. The constant τ_0 depends on the width of the bandpass; t_0 is a group delay, which is supposed to be constant for the relevant frequencies. We assume that the object is illuminated by a single impulse peak emitted at $t = 0$. The (elemental) reflective areas of the object cause this impulse to be scattered and to return with different amplitudes A_n and at different times t_n . The impulses returning from the object are indexed $1 \cdots N$ and are fed into the channel after propagation times t_n .

If excited by a sequence of unit impulses

$$s(t) = \sum_{n=1}^N A_n \delta(t - t_n) \quad (30)$$

the channel will respond with a linear combination of shifted impulse responses according to (29) triggered at different times t_n :

$$u_1(t) = \sum_{n=1}^N A_n h(t - t_n) \quad (31)$$

where

$$h(t - t_n) = D_0 \cos(2\pi f_0[t - t_n])e^{-(t-t_n)^2/\tau_0^2}$$

and D_0 is the gain constant of the channel. The group delay t_0 in (29) is small compared to the propagation delay t_n and is therefore neglected. The purpose of signal preprocessing is the extraction of A_n and t_n from (31). This is done by isolating the envelope represented by the exponential term and a subsequent search for the time and values of the local maxima of $u_1(t)$.

Signal preprocessing starts with a correlation of the channel output $u_1(t)$ with a calibration echo

$$y(t) = \cos(2\pi f_0 t)e^{-t^2/\tau_0^2} \quad (32)$$

realized by convolving these two functions. This operation frees the output signal from noise and, most importantly, detects faint echoes (see Section IV). It can be shown that, after this convolution, the resulting signal $u_2(t)$ may be written as follows:

$$u_2(t) = D_1 \sum_{n=1}^N A_n \cos(2\pi f_0[t - t_n])e^{-(t-t_n)^2/(2\tau_0^2)} \quad (33)$$

where $D_1 = D_0 \tau_0 \sqrt{\pi/2}$. In a second step, the signal is demodulated by taking absolute values of $u_2(t)$. Using $|\cos(x)| = \sqrt{1 + \cos(2x)}/\sqrt{2}$, (33) may be written as:

$$|u_2(t)| = D_1 \sum_{n=1}^N A_n \frac{1}{\sqrt{2}} \cdot \left(1 + \frac{1}{2} \cos(4\pi f_0[t - t_n]) - \frac{1}{8} \cos^2(4\pi f_0[t - t_n]) + \cdots \right) e^{-(t-t_n)^2/(2\tau_0^2)} \quad (34)$$

Filtering away all frequencies $f \geq 2f_0$ yields

$$|u_2(t)| \approx \frac{D_1}{\sqrt{2}} \sum_{n=1}^N A_n e^{-(t-t_n)^2/(2\tau_0^2)}$$

In principle, the shape of the exponential term in (34) is slightly distorted because part of its infinite spectrum is also suppressed. This can be tolerated, however, because most of the signal energy is located at frequencies below $2f_0$.

Finally, thresholding cuts away residual noise. The level of the threshold is generated automatically by observing $|u_2(t)|$ at times where the absence of echoes can be guaranteed. This dynamic adaptation makes a correct recognition of echoes possible even in the presence of ambient noise. In this case, the threshold level is increased automatically, which results in a reduced sensitivity to noise (and to the echoes). It was shown experimentally that axial resolutions of 2 mm and absolute precisions of 0.5 mm may be achieved (for typical outputs of the preprocessing step, see Section IV). A necessary presupposition for measurement precision is, of course, that the propagation medium air is completely undisturbed. However, even in a laboratory, it is difficult to maintain these ideal conditions.

The experiments were carried out with correlation and filtering done in the frequency domain. In the course of our experiments, we found that the quality of the results of the preprocessing procedure as described above do not suffer substantially if the initial windowing operation using the Gaussian window is omitted. This is due to the fact that the form of the $L^2 QZ$ transducer's transfer function at frequencies around the center frequency is quite close to the form of the Gaussian function. The omission of this initial operation saves some amount of computation time; more time can be saved if signal preprocessing is carried out in the time domain on dedicated hardware. More sophisticated model-based signal processing methods as outlined in [45]–[47] have been investigated, but it turned out that the additional resolution achieved will hardly justify their use, particularly if the necessary amount of computation is taken into account. Moreover, if channel parameters vary due to changes in the propagation medium or due to slight alteration of the transducer's transfer function caused by material fatigue, the parameters of the model will not match the actual behavior, making the time-consuming generation of a new set of parameters necessary.

B. Geometric Considerations

We now consider the geometry of the sensor as a whole, including the transmitter, which provides for the illumination of the object. There are several illumination schemes conceivable; in our context, the transmission of a short pulse and subsequent simultaneous reception at a certain number of receiving points promises the fastest speed of recording (Fig. 14). The aperture width D necessary for a certain recognition task depends on the maximum angle from which the transmitted impulse is reflected by the object. On the other hand, the beam width of the outermost receiver must be large enough to receive an echo returning from this angle γ .

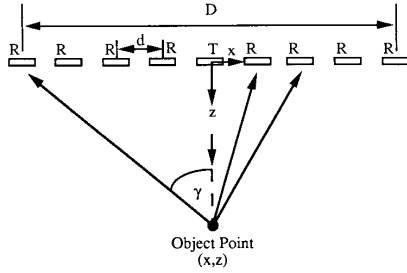


Fig. 14. Data acquisition for multifrequency holography using a single transmitter *T* and several receivers *R* along an aperture of length *D*.

If the object at (x, z) is located below the transmitter, i.e., $x = 0$ (where the sound magnitude is the highest), maximum data acquisition time becomes

$$t_{\max} = \frac{z + \sqrt{z^2 + \frac{D^2}{4}}}{c}$$

which is on the order of milliseconds for typical arrangements.

Unfortunately, many objects of interest will not fit into the rather narrow beam of the transducer. A solution to this problem is the segmentation of the reconstruction area and separate consecutive illumination of each of the segments. An array of transducers for this approach can be constructed as shown in Fig. 15. It consists of a row of alternating receivers and transmitters. The object is illuminated by firing one transmitter after the other and receiving with a constant number of transducers both to the left- and right-hand sides of the current transmitter. If, say, transmitter k was activated, then return echoes are received by elements $k - m$ through $k + m$. Subsequently, transmitter $k + 1$ fires and elements $k - m + 1$ through $k + m + 1$ receive, and so on. Reconstruction of all of these shots then takes place for slices of width d (the segments) for each of the shots, i.e., it is limited to the area where the beam of the transmitter is the strongest. Finally, the stack of images restricted to areas (d, z) is put together to form the entire image of width D . The data acquisition time is multiplied by the number of shots taken, but in practice will remain well below 1 s.

Given the geometry and the nomenclature of Fig. 16, the distance ρ_S between transmitter and object point (x, z) becomes

$$\rho_S = \sqrt{x^2 + z^2}.$$

Introducing the additional delay in propagation due to this distance into (28) we have

$$\Phi(x, z; t) = \int_{-\infty}^{\infty} \frac{z}{\rho \sqrt{\rho}} \Phi'(x', 0; t + \frac{\rho_{SR}}{c}) dx' \quad (35)$$

where

$$\rho_{SR} = \rho + \rho_S = \sqrt{(x - x')^2 + z^2} + \sqrt{x'^2 + z^2}.$$

All potential object points causing an identical delay between

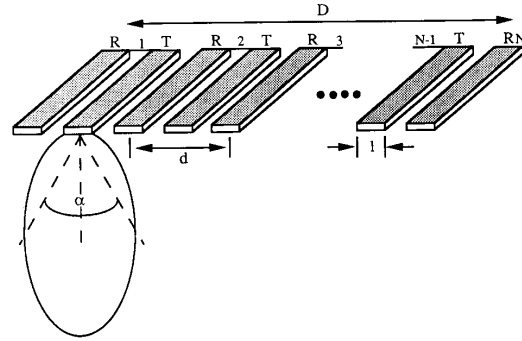


Fig. 15. Array for segmented data acquisition. Transmitting element *T*, receiving element *R*, element size *l*, total array size *D*, beam width α , and element spacing *d*.

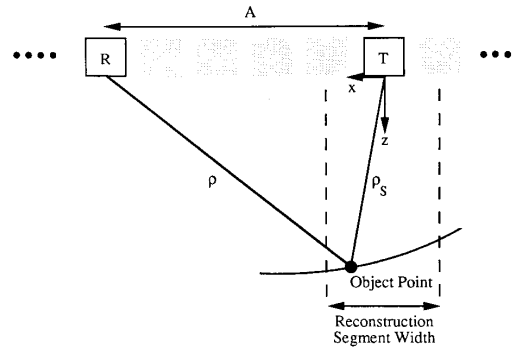


Fig. 16. Segment of an ellipse resulting from single echo recorded by one transmitter-receiver pair.

the transmitter and a fixed receiver are located on an ellipse with the two transducers being the foci. Therefore, the image formation process described by (28) may be viewed as the weighted superposition of number values representing the echo strength along different ellipses. The ellipses corresponding to $n = 1 \cdots N$ echoes received on a fixed aperture point are given by

$$z = \sqrt{\frac{[L^2 + 2Ax - A^2]^2}{4L^2} - x^2} \quad (36)$$

where $L = \rho + \rho_S = ct_n$. Here, t_n is the arrival time of echo n if the transmitter was triggered at $t = 0$, and A is the distance between the foci. For sufficiently large values of z , the geometric weighting factor in the integral of (28) can be neglected and the image formation reduces to a simple addition of echo strengths along elliptic curves. In practice, the transmitter-receiver pair is surrounded by a finite number of ellipses. This number is equal to the number of echoes detected by signal preprocessing. For a mechanical arrangement as depicted by Fig. 16 and if $A \ll L = ct_n$, the curvature of the ellipse inside one reconstruction segment of width d is small enough to be approximated by its tangent. In this case, the slope of the tangent need be computed only once per segment and echo strengths may then be added along a straight line, not along an elliptic curve according to (36). This may reduce the amount of computation necessary.

If the output of the preprocessing step were taken directly as the input of reconstruction, ellipses would have to be curves as broad as the burst length of partial echoes. Instead, the echo signals are seen as distorted unit impulses and are replaced with a function $s(t)$ where

$$s(t) = \begin{cases} C_n, & \text{for } t = t_n \\ 0, & \text{elsewhere} \end{cases}$$

and C_n is the amplitude of the partial echo (as resulting from the search for local maxima), marking the echo strength along the points of ellipse n .

C. Resolution

In a nonideal wavefield reconstruction system, the image of an object is distorted when compared to its true dimensions. With systems that have a limited aperture width, the image of the object becomes smeared, causing two objects placed close together to "melt" into one single object. To specify the resolution, we compute the closest distance between two point objects that the system is able to discriminate. In the case of monofrequency holography, lateral resolution rs_L is found by reconstructing the wave field of a point object. The resulting image is called the point spread function; see [31] for an analytical model of the point spread function along the $(0, z)$ plane and the (x, z_0) plane. The zeros of this function in the lateral direction are a measure for the resolution and, for our geometry, are given by

$$rs_L = \lambda \frac{z_0}{D} \quad (37)$$

where D is the length of the aperture, λ is the wavelength, and z_0 is the distance between the aperture and the object. The axial resolution rs_A of the system is also found by examining the point spread function. Since it has no zeros in the axial direction, rs_A is defined to be at half its maximum value. Then

$$rs_A = \lambda \frac{4z_0^2}{D^2} \quad (38)$$

The range resolution rs_R of the multifrequency system in pulse reflection mode depends on the bandwidth of the transfer channel B and is approximately

$$rs_R \approx \frac{c}{2B} \quad (39)$$

while the lateral resolution can be found [21] to be

$$rs_L \approx \frac{z_0 c}{f_0 D} \quad (40)$$

where in both (39) and (40) c denotes sound velocity. Lateral resolution is on the same order as axial resolution if the aperture size is large enough. In reality, it degrades considerably due to the limited beam width of the transducers and the spacing of transducer elements.

D. Experimental Setup

A schematic of the mechanical setup that was used both for monofrequency and multifrequency holography is shown in

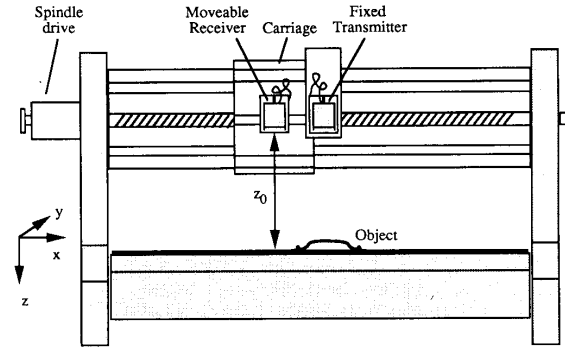


Fig. 17. Mechanical setup used for holography experiments. Transducers were changed according to the experiment that was carried out.

Fig. 17. In the case of monofrequency holography a fixed ultrasonic transmitter continuously irradiated the objects, which, due to the limited axial resolution in the monofrequency case, were placed in one object plane at depth z_0 . The receiver was placed in a moveable carriage; its height z_0 was adjustable. The carriage was moved by a spindle drive under the control of a microcomputer (PC/AT). The experiments were carried out using a set of transducers operating at frequencies of 40 kHz (MuRata MA 40). The objects that were used as reflectors had no structure in the y direction inside the stripe illuminated by the receiver, a necessary precondition if the aperture is only one-dimensional. This was particularly important with the MuRata transducers, which have a large azimuthal radiation angle. Therefore, the objects used here were bar-like, i.e., their structure was uniform in the long dimension and they were about 400 mm long to ensure an undisturbed reflection of the irradiating wave.

The electrical setup used for monofrequency holography is shown in Fig. 18. The transmitter was excited by a power oscillator generating a sinusoidal voltage of the appropriate frequency. It also served as the reference for the vector analyzer (Rohde & Schwarz ZPV). The analyzer compared the transmitted signal to the received signal and output the ratio as a complex value. The results of these comparisons were transferred to the control computer that performed the reconstruction and sent it to a plotter for graphic rendering.

For multifrequency holography the same slide table was utilized, but the transducers were replaced with a set of L^2QZ transducers (see Fig. 19). With unsegmented multifrequency holography, the transmitter was fixed and the receiver was moveable. In the case of segmented holography, as outlined in Subsection III-B, the transmitter remained at one location while the receiver was moved, and consecutive shots were taken for a single segment. To acquire data for the next segment, the transmitter was moved manually by the segment width, and the sequence of shots was repeated. The power oscillator was replaced with a pulse generator, which supplied impulses of a duration $t_p < 10 \mu s$ and an amplitude $U_p > 200 V$. Since the L^2QZ receiver provided output voltages of only a fraction of 1 mV, a special low-noise

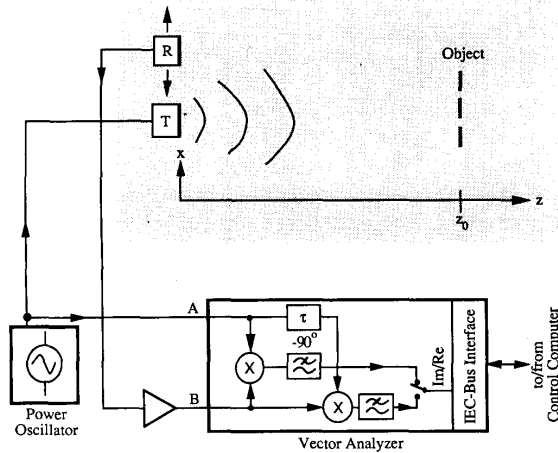


Fig. 18. Schematics of the setup for monofrequency holography.

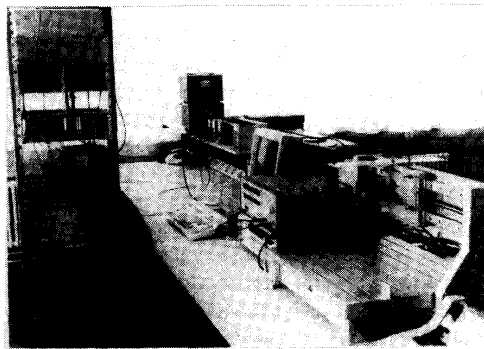


Fig. 19. Multifrequency apparatus showing L^2OZ transducers mounted on slide table, with the pulse generator and control computer on the right. Transient recorder and power supplies are on the left.

amplifier operating at frequencies up to 1 MHz and matched to the transducer parameters had to be developed. The amplifier was connected to a one-shot transient recorder sampling the input signal at 8 MHz and digitizing it to 8 bits. The total size of the memory was 32 kbyte; thus, the maximum time for filling the entire storage with data was 4 ms. Within this time interval ultrasound travels about 1.35 m; hence, the round-trip distance between transmitter, object point, and receiver must not exceed this limit.

IV. RESULTS

A. Monofrequency Holography

Fig. 20 shows the geometrical arrangement for imaging a single reflector. A steel bar—30 mm wide and 400 mm long—was illuminated by a continuous sound wave field at a frequency of 40 kHz corresponding to a wave length of $\lambda \approx 8$ mm. The aperture was limited to $D = 370$ mm. Along the aperture, the sound field was recorded at 256 points that were equally spaced at a distance $d = 1.4$ mm. In Fig. 21 the complete recorded hologram is shown, i.e., its real and imaginary part as measured on the aperture at $z = 0$. The

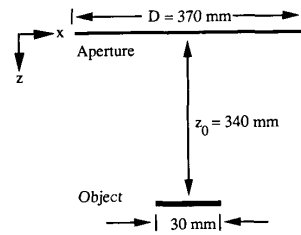


Fig. 20. Single reflector scene. The width of the object in the lateral direction is 30 mm. The height of the object is 400 mm, i.e., perpendicular to the (x, z) plane, the object extends from $y = -200$ mm to $y = 200$ mm, with the position of the aperture being at $y = 0$.

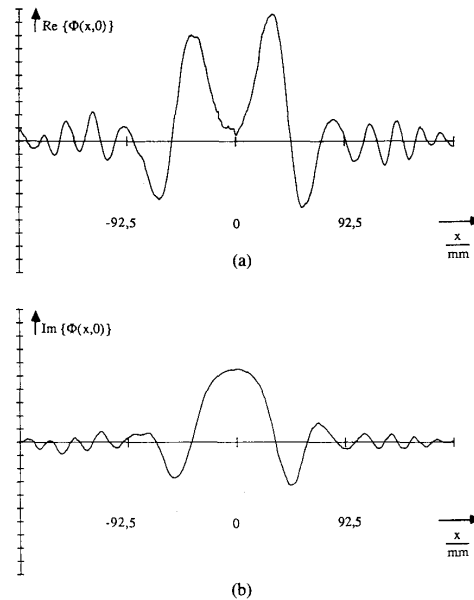


Fig. 21. Hologram recorded when single reflector of Fig. 20 is used. (a) Real part. (b) Imaginary part.

result of the reconstruction process for $z = z_0$ (the depth of the object plane) is shown in Fig. 22. As expected, the magnitude of the sound field is high at the location of the reflector, everywhere else it is nearly equal to zero. The width of the magnitude peak in Fig. 22 matches the width of the object quite well if the resolution limit of the method (see (37)) is considered. The depth resolution is demonstrated in Fig. 23 by reconstructing the wave field at different depth levels and plotting its magnitude over the (x, z) plane. Between the object and the aperture, the magnitude of the field falls off very slowly, by far not as rapidly as necessary for useful axial recognition. Due to the averaging during the recording process, it falls off more slowly than one would theoretically expect. To further explore the ability of the method to resolve objects laterally, three reflectors (8, 20, and 8 mm wide) were placed next to one another in one plane with a 12-mm gap in the lateral direction between them. All of these reflectors were 400 mm long. The resulting image at $z_0 = 340$ mm is shown in Fig. 24.

Despite its ability to recognize lateral structures when the

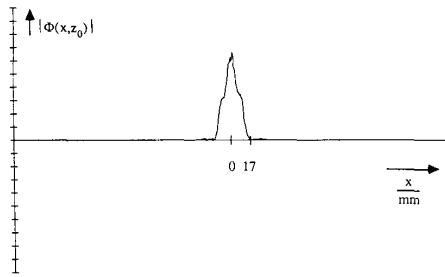


Fig. 22. Sound field magnitude resulting from the reconstruction of the hologram of Fig. 21.

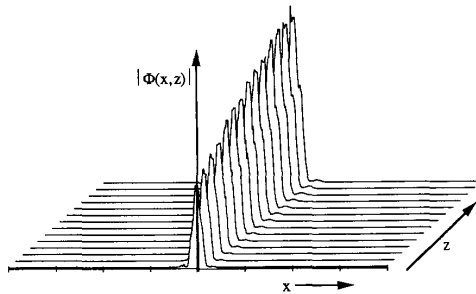


Fig. 23. Plot of sound field magnitude over (x, z) plane. Distance between reconstruction depths is 2 cm with first line being at $z = 11$ cm.

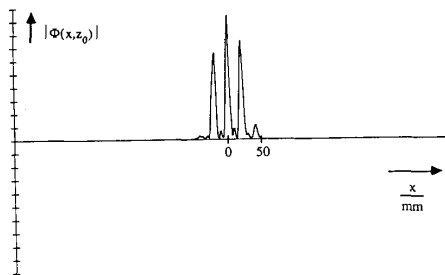


Fig. 24. Sound field magnitude at object depth resulting from three-reflector scene.

distance z_0 is known, the range of applications of monofrequency holography seems to be rather limited if no extra hardware for the determination of the distance between aperture and object is added. Moreover, it turned out during our experiments that even minimal air currents, as generated, for example, by cooling fans in the environment of the object, may disturb the ongoing measurement to such a degree that the result is completely useless. The reason for this is easy to see if one recalls that complete stationarity was assumed for the method and no time dependence of measured data was admitted. Both the amplitude and the phase must remain absolutely stable between measurements. Now, if the propagation times varies only by $12.5 \mu\text{s}$, at 40 kHz a phase shift of π will follow, which inverts the result and precludes sensible further processing. This must be compared to a total round-trip time of more than 2 ms.

To summarize, monofrequency holography does have some advantages over pulse echo methods, namely, noise immu-

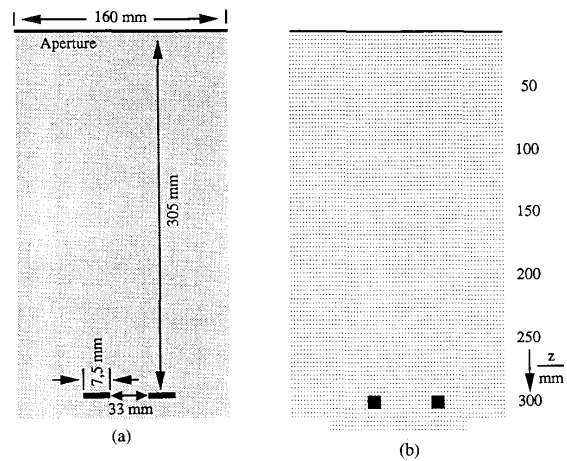


Fig. 25. (a) Geometry and (b) reconstruction result for dual reflector scene, multifrequency holography.

nity, a very low data volume, and lateral resolution. It permits the use of very efficient narrow-band transducers making long-range sensors possible. It suffers, however, from serious drawbacks pertaining to depth resolution and high sensitivity to fluctuations in the propagation medium.

B. Multifrequency Holography

To explore the potential of the multifrequency approach, several objects of different surface structure were imaged. Reconstruction using (28) was carried out on a grid consisting of rectangular elements whose dimensions were chosen differently depending on the desired maximum resolution. The sound field was computed for each element, and a suitable threshold was applied to it. If the sound field exceeded the threshold, the raster element was marked as belonging to the object contour. Figs. 25 and 26 show the results for two different scenes consisting of simple objects. In Fig. 25 two plane objects 7.5 mm wide were imaged using a quadratic element size of $10 \times 10 \text{ mm}^2$ for reconstruction. The resulting picture shows that the object position is recognized correctly within the chosen resolution limit both in the axial and the lateral directions. The reconstruction of the object of Fig. 26, which was turned into an oblique position with respect to the direction of sound propagation, also yields a correct image. The raster element size was reduced to $5 \times 5 \text{ mm}^2$ here. Note that the system cannot recognize anything behind the surfaces closest to the aperture. The three raster elements behind the location of the reflector in the reconstruction result (bottom of Fig. 26) are marked only because the magnitude was so high that it "spilled" into the neighboring elements. Given the small aperture of Figs. 25 and 26, an increase of the inclination of the object will direct most of the reflected signal energy past the aperture and produce a blurred image. If greater inclinations are to be recognized as well, the aperture width must be increased.

In both cases echo data were acquired using only one transmitter and by recording at 17 locations where $d = 10$ mm (nonsegmented approach). Examples of results from the

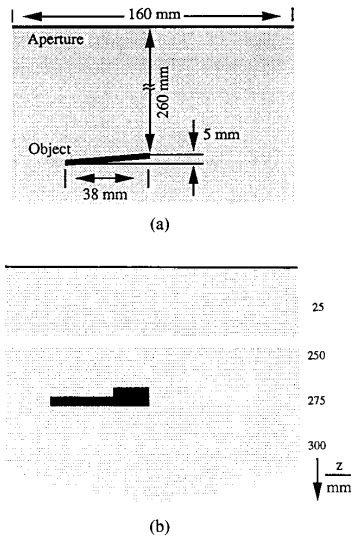


Fig. 26. (a) Geometry and (b) reconstruction result for oblique reflector scene, multifrequency holography.

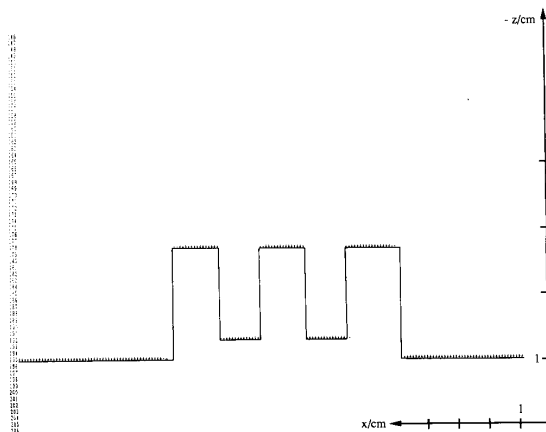


Fig. 27. Reconstruction result of multifrequency holography, segmented data acquisition. Segment width is 3 mm. Solid line indicates true object dimensions. Character distance marks a lateral distance of 1 mm. Numbers on the left side indicate rows of reconstruction raster. Distance between rows is 1 mm.

segmented approach for data acquisition are shown in Figs. 27 to 29. The segment width (spacing of transmitter positions) was $d = 3$ mm in Fig. 27 and 10 mm in Figs. 28 and 29. The solid line indicates true object contours. Apart from some overshoots in the lateral direction, the surfaces that are visible to the system are recognized accurately. Note the varying resolution scale in each of the figures. The lateral overshoots can be reduced at the expense of the data acquisition time if the segment width is reduced. The images in Figs. 27-29 result from "real-world" objects used in the automotive industry (see Fig. 30). The lines along which the cross-sectional images were taken are indicated by the white stripes on the objects.

A typical sequence of transients received at consecutive aperture points is shown in Fig. 31. The functions resulting

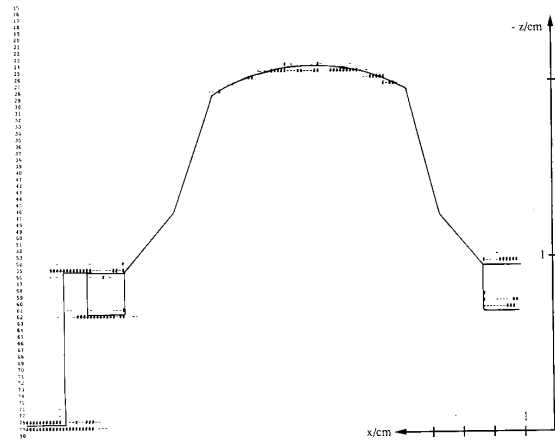


Fig. 28. Reconstruction result of multifrequency holography, segmented data acquisition. Segment width is 10 mm. Solid line indicates true object dimensions. Character distance marks a lateral distance of 1 mm. Numbers on the left side indicate rows of reconstruction raster. Distance between rows is 0.375 mm.

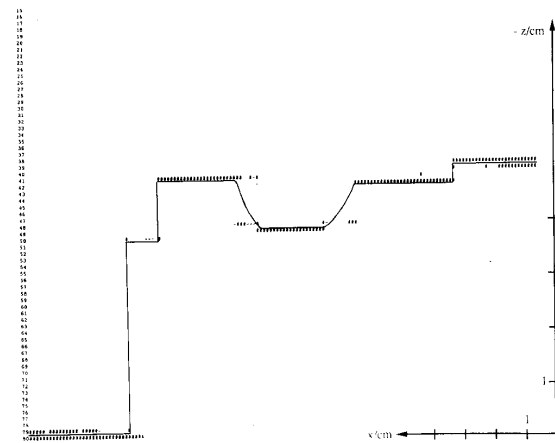


Fig. 29. Reconstruction result of multifrequency holography, segmented data acquisition. Segment width is 10 mm. Solid line indicates true object dimensions. Character distance marks a lateral distance of 1 mm. Numbers on the left side indicate rows of reconstruction raster. Distance between rows is 1.25 mm.

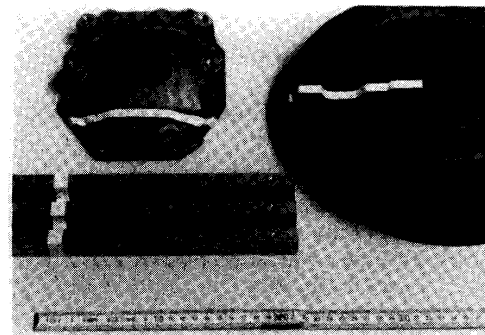


Fig. 30. The objects from the automotive industry that were used to generate the images of Figs. 27-29. The white line on each of the objects indicates the path along which the transducers were moved.

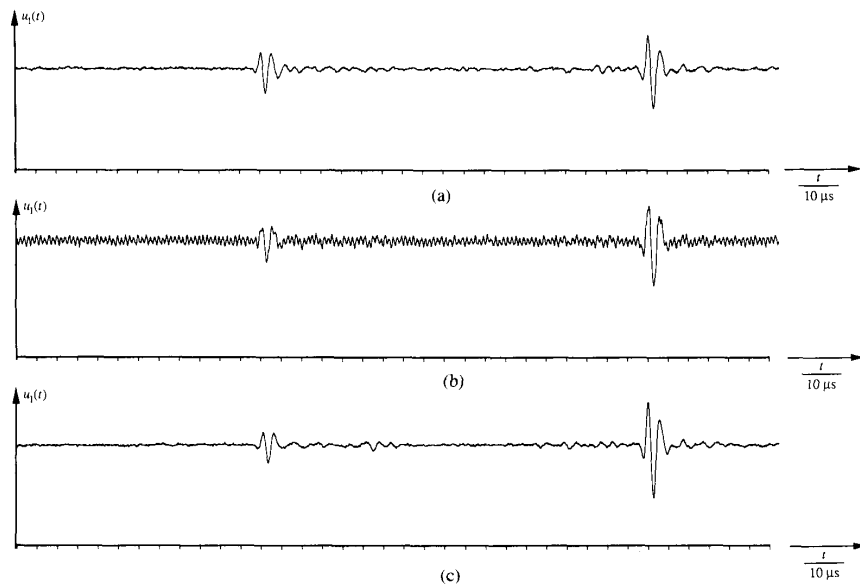


Fig. 31. Sequence of transients recorded during data acquisition of multifrequency holography. (a) and (c) are undisturbed; (b) is disturbed by RF interference.

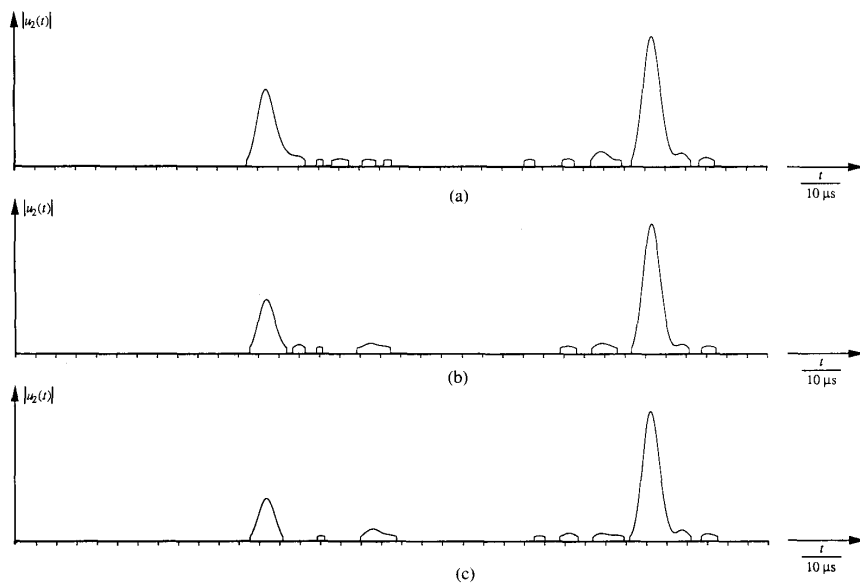


Fig. 32. Transients of Fig. 31 after signal preprocessing and thresholding.

after application of the signal preprocessing algorithm and after thresholding are shown in Fig. 32. Although the second of the transients is noisy (due to RF interference), even faint echoes not visible to a human observer in Fig. 31 become apparent to the eye in Fig. 32.

Due to the fact that the array of transducers was simulated by only two movable transducers, the total acquisition time was between 30 s and several minutes depending on the number of segments. Processing the acquired data and gener-

ating a complete image took about 5 min on a PC/AT; most of this time was spent on signal preprocessing. As mentioned before, the acquisition time can be reduced to several milliseconds if an array of wide-band transducers according to Fig. 15 is available. The processing time may also be reduced drastically if dedicated hardware is used. In particular, much of the preprocessing can be performed by analog circuitry. Such hardware would make real-time imaging possible, i.e., a continuous image generation rate of up to 10

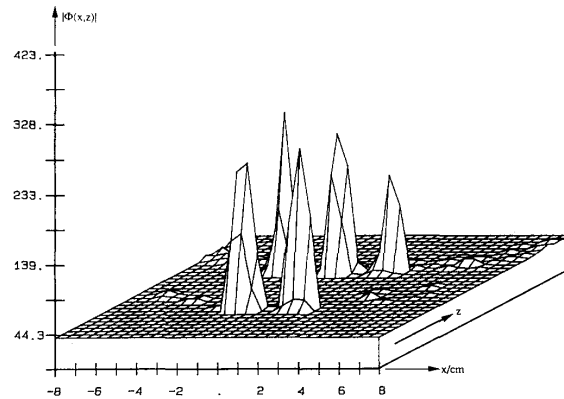


Fig. 33. Reconstructed sound field magnitude of five reflector scene, multifrequency holography. Change of the threshold value will influence output object contours.

TABLE I
SUMMARY OF EXPERIMENTAL RESULTS
(The accuracy is the maximum distance between a true object point and its mapping in the image when a single object is imaged.)

	Monofrequency Holography	Multifrequency Holography	Segmented Multifrequency Holography
Type of transducers	MuRata MA 40	Siemens L ² QZ	Siemens L ² QZ
Nominal center frequency of transducers	40 kHz	200 kHz	200 kHz
Bandwidth of transducers	6 kHz	200 kHz	200 kHz
Aperture length	370 mm	160 mm	220 mm
No. of receiving points of the aperture	256	17	17 (for each segment)
Distance between receiving points	1.4 mm	10 mm	10 mm
No. of transmitting points of the aperture	1	1	21
Distance between transmitting points	—	—	3 or 10 mm
Resolution			
axial	—	< 3 mm	< 3 mm
lateral	< 20 mm	< 30 mm	< 10 mm
Accuracy			
axial	—	1 mm	1 mm
lateral	< 10 mm	< 10 mm	< 5 mm

images per second seems to be easily achievable. This is more than is necessary in typical robot assembly tasks.

For the example images presented above, the object contours were generated by applying a constant threshold on the reconstructed sound field. The determination of a suitable threshold level is crucial to correct object recognition. This is illustrated by Fig. 33 where the magnitude of the sound field echoed from five 10-mm-diameter steel poles is plotted over the (x, z) plane. Within certain limits, the choice of the threshold influences the size of the object contour directly: The greater the threshold level, the smaller appears the object; on the other hand, too low a threshold will result in insufficient noise suppression. The level for the above scenes was generated successfully using simple heuristic rules, but both for the practical use and for higher resolutions a greater understanding of how object structure, object distance, and object surface interact to form a particular echo will be necessary. Table I summarizes the parameters and results of the experiments we carried out.

The automatic handling of solid objects requires sensing systems that locate the position of the target object exactly. This is in sharp contrast to many other applications of ultrasonics where the images output by the system are subjected to the interpretation of a human observer, thereby implicitly making use of his or her *a priori* knowledge and experience about the behavior of the imaging system, the anticipated position of the object, and the importance of its details. In our case, however, the intervention of humans for object segmentation is obviously impossible. It is essential for the system to find the significance of objects and their true dimensions fully automatically.

V. CONCLUSIONS

We have proposed the use of ultrasonic holography for the recognition of solid objects in order to facilitate the process of automatic determination of both object distance and structure. We have demonstrated the feasibility of the method by experimental verification. Unlike other methods based on

ultrasonics, holography makes use of the complete information provided by sound field echoes returning from three-dimensional space. The recording of this information along a linear antenna permits the generation of object shape descriptions in the lateral direction, i.e., perpendicular to sound propagation, and for objects of cylindrical symmetry. The recording of time-dependent echoes in the multifrequency case additionally permits the recognition of object details in the depth direction and an accurate determination of their position in space.

Our experimental results indicate that the method holds the potential to be an important supplement to optical vision systems and that in some cases it may even be a substitute for them. Possible applications include tasks such as the handling of similar objects of different heights or bin picking, where range information is indispensable and tasks where insufficient lighting and/or properties of the object surface precludes the use of optical images. Inspection of assembled parts for completeness is a possible application as is the control of robot end effectors during approach/deproach of the target object. The combination of a sensor based on the principle of multifrequency holography with the Belgrade/USC dextrous robot hand [48]–[50] is being studied. Here, the preshaping of the hand before it is brought in contact with the object to be grasped is to be controlled.

The holographic approach offers several advantages over vision systems including its use of simple recording devices, generally low hardware cost, and its inherent ability to determine range. The latter obviates the need to extract the depth dimension from its two-dimensional projections. Since the image is focused synthetically point by point in the computer memory, resolution is uniform over the entire depth range. However, due to the specularly of ultrasonic reflections, parts of an object visible to an optical system may not be detectable by the ultrasonic sensor (and vice versa).

A resolution of better than 3 mm was shown to be achievable in the depth direction while in the lateral direction our experimental geometry provided for a resolution of about 10 mm. The resolution limit results from fluctuations in the medium (air) and is approximately 1 mm given a propagation distance of more than 10 cm [21].

A combination of an ultrasonic holographic sensor and a camera vision system may lend itself to all those tasks requiring high accuracy in the lateral direction. Since the behavior of both systems is known mathematically and they complement each other, the fusion of their data will be useful. This might be carried by a rule-based system derived from the mathematical model of the sensor, but not from possible constellations of objects in the environment of the sensor.

In conclusion, to further exploit the potential of the holographic approach, more work needs to be directed along the following lines:

- 1) development and construction of an array of efficient broad-band transducer elements,
- 2) algorithms for thresholding depending on image content,

- 3) dedicated hardware designed to make use of parallelism inherent in reconstruction formulas, and
- 4) fusion with sensors based on principles other than sound wave propagation.

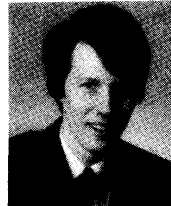
ACKNOWLEDGMENT

The author gratefully acknowledges the contributions of G. Hommel and J. Kutzner. Thanks also go to G. Bekey, A. Rozek, J. Meinkoehn, and D. Jacobs and to the anonymous reviewers for their valuable comments.

REFERENCES

- [1] U. Ahrens, "Möglichkeiten und Probleme der Anwendung von Luftultraschall in der Montage- und Handhabungstechnik," *Roboter-systeme*, vol. 1, no. 1, 1985.
- [2] J. Knight, S. Pomeroy, H. Dixon, and M. Wybrow, "Ultrasonic distance measuring and imaging systems for industrial robots," *Robotics*, vol. 3, pp. 181–188, 1987.
- [3] G. Drunk, "Sensors for mobile robots," in *Sensors and Sensory Systems for Advanced Robots, ASI Series F*, vol. F43. Berlin: Springer-Verlag, 1987.
- [4] J. Borenstein and Y. Koren, "Obstacle avoidance with ultrasonic sensors," in *Proc. IEEE Int. Conf. Robotics Automat.*, 1985.
- [5] R. Madarasz, L. Heiny, R. Cromp, and N. Mazur, "The design of an autonomous vehicle for the disabled," *IEEE J. Robotics Automat.*, vol. 4, no. 2, 1988.
- [6] A. Elfes, "Sonar-based real-world mapping and navigation," *IEEE J. Robotics Automat.*, vol. RA-3, 1987.
- [7] S. Walter, "The sonar ring—Obstacle detection for a mobile robot," in *Proc. IEEE Conf. Robotics Automat.*, 1987.
- [8] J. Crowley, "World modeling and position estimation for a mobile robot using ultrasonic ranging," in *Proc. IEEE Int. Conf. Robotics Automat.*, 1989.
- [9] J. Richardson, K. Marsh, J. Schoenwald, and J. Martin, "Acoustic imaging of objects in air using a small set of transducers," in *Proc. IEEE Ultrasonics Symp.*, 1984.
- [10] U. Ahrens and A. Langen, "Ultraschallscanner—Ein neues System zur Roboterführung," in *VDI-Berichte Nr. 598*. Düsseldorf, Germany: VDI-Verlag, 1986.
- [11] M. Brown, "Locating object surfaces with an ultrasonic range sensor," in *Proc. IEEE Int. Conf. Robotics Automat.*, 1985.
- [12] S. Gruber, "An inexpensive multi-sensor controlled end effector for a dumb robot," in *Proc. IEEE Int. Workshop on Robotics—Trends, Technol. Applications*, 1987.
- [13] L. Kay, "Airborne ultrasonic imaging of a robot work space," *Sensor Rev.*, vol. 5, no. 1, 1985.
- [14] G. Miller, R. Boie, and M. Sibilia, "Active damping of ultrasonic transducers for robotic applications," in *Proc. IEEE Conf. Robotics Automat.*, 1984.
- [15] J. Schoenwald, J. Martin, and L. Ahlberg, "Acoustic scanning for robotic range sensing and object pattern recognition," in *Proc. IEEE Ultrasonics Symp.*, 1982.
- [16] J. Schoenwald, "Acoustic range sensing for robotic control," in *Sensor Devices and Systems for Robotics, ASI Series F*, vol. F52. Berlin: Springer-Verlag, 1989.
- [17] J. Martin, R. Ceres, J. No, and L. Calderón, "Adaptive ultrasonic range finder for robotics," in *Sensor Devices and Systems for Robotics, ASI Series F*, vol. F52. Berlin: Springer-Verlag, 1989.
- [18] A. Acampora and J. Winters, "Three-dimensional ultrasonic vision for robotic applications," *IEEE Trans. Pattern Anal. Machine Intell.*, vol. 11, no. 3, 1989.
- [19] R. Kuc and M. Siegel, "Physically based simulation model for acoustic sensor robot navigation," *IEEE Trans. Pattern Anal. Machine Intell.*, vol. PAMI-9, no. 6, Nov. 1987.
- [20] D. Jaffe, "Polaroid ultrasonic ranging sensors in robotics applications," *Robotics Age*, pp. 23–30, Mar. 1985.
- [21] J. Löschberger, "Ultraschall-Sensor-System zur Bestimmung axialer und lateraler Strukturen mit Hilfe bewegter Wandler zum Einsatz in der industriellen Automation," Ph.D. dissertation, Munich, Germany, 1987.
- [22] V. Mágóri, "Ultraschall-Distanzsensoren zur Objektidentifizierung und Lageerkennung," in *VDI-Bericht Nr. 509*. Düsseldorf, Germany: VDI-Verlag, 1984.

- [23] J. Ylitalo, E. Alasaarela, and J. Koivukangas, "Ultrasound holographic B-scan imaging," *IEEE Trans Ultrason. Ferroelectrics Frequency Control*, vol. 36, no. 3, 1989.
- [24] C. Schueler, H. Lee, and G. Wade, "Fundamentals of digital ultrasonic imaging," *IEEE Trans. Sonics and Ultrason.*, vol. SU-31, no. 4, 1984.
- [25] J. Sutton, "Underwater acoustic imaging," *Proc. IEEE*, vol. 67, no. 4, 1979.
- [26] J. Kutzner and H. Wüstenberg, "Akustische Holographie in Tandemanordnung, ein Hilfsmittel zur Fehleranzeigeninterpretation in der Ultraschallprüfung," *Materialprüfung*, vol. 18, no. 12, 1976.
- [27] —, "Akustische Linienholographie, ein Hilfsmittel zur Fehleranzeigeninterpretation in der Ultraschallprüfung," *Materialprüfung*, vol. 18, no. 6, 1976.
- [28] G. Kino, "Acoustic imaging for nondestructive evaluation," *Proc. IEEE*, vol. 67, no. 4, 1979.
- [29] S. Haykin, *Array Signal Processing*. Englewood Cliffs: Prentice-Hall, 1985.
- [30] E. Williams, J. Maynard, and E. Skudrzyk, "Sound source reconstruction using a microphone array," *J. Acoust. Soc. Amer.*, vol. 68, no. 1, 1980.
- [31] J. Kutzner, *Grundlagen der Ultraschallphysik*. Stuttgart, Germany: Teubner, 1983.
- [32] E. Skudrzyk, *The Foundations of Acoustics*. New York: Springer-Verlag, 1971.
- [33] J. Goodman, *Introduction to Fourier Optics*. New York: McGraw-Hill, 1968.
- [34] A. Macovski, "Ultrasound imaging using arrays," *Proc. IEEE*, vol. 67, no. 4, 1979.
- [35] S. Pillai, *Array Signal Processing*. New York: Springer-Verlag, 1989.
- [36] J. Fitch, *Synthetic Aperture Radar*. New York: Springer-Verlag, 1988.
- [37] W. Neubauer, "A summation formula for use in determining the reflection from irregular bodies," *J. Acoust. Soc. Amer.*, vol. 35, no. 3, 1963.
- [38] D. Johnson, "Model for predicting the reflection of ultrasonic pulses from a body of known shape," *J. Acoust. Soc. Amer.*, vol. 59, no. 6, 1976.
- [39] N. Haines and D. Langston, "The reflection of ultrasonic pulses from surfaces," *J. Acoust. Soc. Amer.*, vol. 67, no. 5, 1980.
- [40] K. Trivedi, *Probability and Statistics with Reliability Queuing and Computer Science Applications*. Englewood Cliffs: Prentice-Hall, 1982.
- [41] P. Beckman and A. Spizzichino, *The Scattering of Electromagnetic Waves from Rough Surfaces*. Dedham, MA: Artech House, 1987.
- [42] P. Kleinschmidt and V. Mágori, "Ultrasound robotic sensors for exact short range distance measurement and object identification," in *Proc. IEEE Ultrasonics Symp.*, 1985.
- [43] M. Rossi, *Acoustics and Electroacoustics*. Dedham, MA: Artech House, 1988.
- [44] *Data Sheet Ultrasonic Transducers*, muRata Corp., Kyoto, Japan, Cat. No. S 04E-4, 1986.
- [45] T. Miyashita, H. Schwetlick, and W. Kessel, "Recovery of the ultrasonic impulse response by spectral extrapolation," *Acoustical Imaging*, vol. 13. New York: Plenum, 1985.
- [46] D. Oldenburg, T. Scheuer, and S. Levy, "Recovery of the acoustic impedance from reflection seismograms," *Geophysics*, vol. 48, no. 10, 1983.
- [47] T. Ulrych and T. Bishop, "Maximum entropy spectral analysis and autoregressive decomposition," *Rev. Geophys. Space Phys.*, vol. 13, no. 1, 1975.
- [48] G. Bekey, R. Tomovic, and I. Zeljkovic, "Control architecture for the Belgrade-USC hand," in *Dextrous Robot Hands*. New York: Springer-Verlag, 1989.
- [49] R. Tomovic, "Advances in the design of autonomous dextrous hands," *Int. J. Robotics Comp. Integr. Manufact.*, 1990.
- [50] M. Rakić, "Multifingered hand with selfadaptability," *Int. J. Robotics Comp. Integr. Manufact.*, vol. 5, no. 2/3, 1989.
- [51] J. Schmolke, D. Hiller, H. Emert, J. Schaefer, and G. Gräbner, "Generation of optimal input signals for ultrasound pulse echo systems," in *Proc. IEEE Ultrasonics Symp.*, 1982.



Alois C. Knoll (M'88) received the M.S. degree in electrical engineering from the University of Stuttgart, Germany, in 1985 and the Ph.D. degree in computer science from the Technical University of Berlin, Germany, in 1988.

He is currently a Wissenschaftlicher Assistent (Assistant Professor) in the Department of Computer Science at the Technical University of Berlin. His research interest is primarily in the area of computer vision with an emphasis on range image generation. He also does work in the field of code generation for digital signal processors.

Dr. Knoll is a member of the German Society for Computer Science (Gesellschaft für Informatik (GI)) and an organizer of the 1991 GI/VDI joint conference on real-time data processing.